CrossMark
←click for updates

Synergistic effects from graphene and carbon nanotubes endow ordered hierarchical structure foams with a combination of compressibility, super-elasticity and stability and potential application as pressure sensors†

Jun Kuang,[a,b] Zhaohe Dai,[a,b] Luqi Liu,*[a] Zhou Yang,[c] Ming Jin[c] and Zhong Zhang*[a]

Nanostructured carbon material based three-dimensional porous architectures have been increasingly developed for various applications, e.g. sensors, elastomer conductors, and energy storage devices. Maintaining architectures with good mechanical performance, including elasticity, load-bearing capacity, fatigue resistance and mechanical stability, is prerequisite for realizing these functions. Though graphene and CNT offer opportunities as nanoscale building blocks, it still remains a great challenge to achieve good mechanical performance in their microarchitectures because of the need to precisely control the structure at different scales. Herein, we fabricate a hierarchical honeycomb-like structured hybrid foam based on both graphene and CNT. The resulting materials possess excellent properties of combined high specific strength, elasticity and mechanical stability, which cannot be achieved in neat CNT and graphene foams. The improved mechanical properties are attributed to the synergistic-effect-induced highly organized, multi-scaled hierarchical architectures. Moreover, with their excellent electrical conductivity, we demonstrated that the hybrid foams could be used as pressure sensors in the fields related to artificial skin.

Introduction

Because of the essential roles played by cellular materials in engineering and biomechanical applications, advanced foam technologies have been heavily involved in the development of new cellular materials by tuning their building blocks to meet the increasing demands for high-performance materials.[1–5] In this field, nanostructured carbon materials, such as carbon nanotubes (CNT) and graphene, which possess the combination of extraordinary mechanical, electrical and thermal properties, hold great promise as exceptional nanoscale building blocks for constructing macroscopic bulk cellular solids.[5–12] Recently, a variety of techniques, such as sol–gel,[6,13–15] hydrothermal,[9,16] and chemical vapor deposition methods,[11,12] have been developed to fabricate various CNT and graphene based cellular solids with multi-functionality, temperature-invariant

performance and ultralow density. However, despite the super elasticity and strength of CNT and graphene building blocks, most of the prepared macroscopic porous architectures are generally brittle with low compression resilience ratios because the microstructural features also dominate the bulk mechanical response.[6,9,12–14,16] Thus, the efficient assembly of nanostructured carbon foams with appropriate structure is the key to fully realize the potential of building blocks in macroscopic architectures and achieve excellent mechanical compressibility, elasticity and stability.

Sustained efforts for innovation have led to the development of CNT and graphene based porous macrostructures with ordered and hierarchical honeycomb-like structures as well as remarkable mechanical resilience. For instance, unlike the isotropic graphene or CNT aerogels formed by random stacking, which are easily collapsed when subjected to compressive deformation, particularly at large strain level,[6,9,12–14,16] the ultra-light free standing multi-walled nanotube aerogels with an ordered honeycomb-like structure, fabricated by a unidirectional freeze-casting approach, have shown excellent compression recoverability.[8] In addition, following the similar technique, Li D. and co-workers[10] fabricated biomimetic honeycomb-like hierarchical graphene based cellular foams by carefully controlling the carbon/oxygen atomic ratio in par-

[a]CAS Key Laboratory of Nanosystem and Hierarchical Fabrication, National Center for Nanoscience and Technology, Beijing 100190, China. E-mail: liulq@nanoctr.cn, zhong.zhang@nanoctr.cn
[b]University of Chinese Academy of Sciences, Beijing 100049, China
[c]School of Materials Science and Engineering, University of Science and Technology of Beijing, Beijing 100083, China
†Electronic supplementary information (ESI) available. See DOI: 10.1039/c5nr00841g

tially reduced graphene oxide sheets. Even though the specific elastic bending stiffness of a plate structure is intrinsically inferior to that of tubular counterparts, the obtained graphene cellular foam still possessed an excellent compression resilience, which was attributed to the ordered structure. Given the fact that the effective properties of cellular materials are defined by both the intrinsic properties of the solid constituents and their structural geometry, we expect that nanostructured material foams would exhibit the expected mechanical performance if the mechanical properties of the solid constituents in the foams could be enhanced along with the structure in this ordered, hierarchical manner.

Previous research advances have attempted to integrate the unique properties of the individual graphene sheets and carbon nanotubes into one-dimensional fibers and two-dimensional (2D) films for practical applications.[17–19] Synergistic effects were observed in hybrid materials of the graphene and CNT, which endowed them with greatly improved electrical, thermal conductivity and, especially, mechanical properties, compared with those made of the individual components. Considering that the three-dimensional (3D) nanocarbon-based foams usually consist of 2D cell walls, the synergetic enhancement of the mechanical performance is expected in hybrid foams constructed by both CNT and graphene. Recently, attempts to combine CNT and graphene have been made to fabricate 3D hybrid cellular solids; however, most of them are focused on electrochemical properties, such as capacity, and only a few reports that address their mechanical response exist.[20–25] For instance, Gao and co-workers fabricated an ultra-flyweight carbon aerogel through building a framework with giant graphene flakes and CNT building blocks. However, the randomly organized structures in their materials, caused by isotropic properties, behaved as a negative unloading stress when the material was subjected to compression, indicating incomplete elasticity.[24] Thus, fabricating CNTs and graphene hybrid foams in a structurally ordered manner and synergistic combination of mechanical compressibility, elasticity and stability to effectively harness the extraordinary mechanical properties of building blocks still remains a challenge.

Herein, we fabricated CNT/graphene hybrid foams with highly ordered hierarchical architectures by applying a unidirectional freeze-casting method. The as-prepared hybrid foam shows an ordered honeycomb-like structure, in which graphene and CNT components are well interwoven and stacked within the cell wall. Symmetrical mechanical tests on these hybrid foams revealed their excellent properties of combined high specific strength, elasticity, compressibility, and dynamic mechanical stability when compared with neat CNT or graphene foams, which cannot be achieved by graphene/CNT hybrid foams with poorly organized structures.[24] Such remarkable mechanical performance is attributed to the synergistic-effect-induced highly organized, multi-scaled hierarchical architectures at different levels, which provide enhanced cell wall strength and stability. Finally, combining with its electrical conductivity, the hybrid foam shows its potential as a flexible pressure sensor. We further demonstrated its potential application in artificial skin fields by integrating hybrid foams into pixel arrays.

Experimental section

Materials

Graphite powder with a size of 20 μm was purchased from Qingdao Yingshida Graphite Co. Ltd. MWCNT (6–8 nm in diameter, up to 50 μm in length, and purity >93 wt%, FloTube-TM7000) was bought from CNano Technology Ltd. Analytical grade $NaNO_3$, $KMnO_4$, 98% H_2SO_4, 69% HNO_3 and 30% H_2O_2 were purchased from Beijing Chemical Works and were used directly without further purification.

Fabrication of CNT, graphene and hybrid foams

GO was prepared by a modified Hummers method.[26] The prepared GO suspension of one of the various concentrations was poured into a Teflon cubic container with a stainless steel bottom. The unidirectional growth of ice from the bottom to the upper face occurred when the stainless steel bottom of the container was immersed in liquid nitrogen. The frozen GO suspension was then transferred into a freeze-drying vessel (−50 °C and 20 Pa) and freeze-dried for 24 h to obtain a macroporous GO foam. To obtain the graphene foam, the GO foam was placed in a tube furnace and annealed at 800 °C for 3 h under an argon atmosphere.

o-CNT (chemically oxidized CNT) was synthesized according to a chemical method reported in the literature[27] but with short oxidizing time, *i.e.*, the CNT was refluxed in a mixture of concentrated H_2SO_4 and HNO_3 (3 : 1 by volume) for only 15 min, and then collected by repeated centrifuging and washing with deionized water. Finally, we obtained aqueous o-CNT. In this step, the oxygen content of o-CNT is important for the properties of the final foam; lower content would render the foam with better mechanical properties. Following the similar procedures to those for making graphene foam, CNT foams were obtained.

By mixing the two solutions together at different weight ratios and following the above-mentioned methods, hybrid foams were obtained.

Characterization

The microstructures and morphologies of the as-prepared foams were characterized by SEM (HITACHI S4800). Spectral analysis of GO and o-CNT was performed by FTIR spectroscopy (Spectrum One, PE, US). A dynamic mechanical analyzer (TA, DMA Q800) was used to evaluate the mechanical performances of the foams. The dimensions of the tested samples were $1 \times 1 \times 1$ cm^3. We combined a home-made mechanical tester and SEM (HITACHI S3400) to observe the *in situ* compressive behaviors of the foams. Electrical properties were tested using a Keithley 4200 SCS in the four-probe mode. The top and bottom surfaces of the foam were coated with a uniform layer of silver paste, and the side faces were coated with two strips

of silver paste. Four silver wires were respectively connected to these areas of silver paste. For electromechanical tests, the top and bottom surfaces of the ReG foam were coated with a uniform layer of silver paste and connected by silver wires. During the compression process, the electrical resistance (Keithley 4200 SCS under a bias of 10 mA) was recorded simultaneously.

Results and discussion

Built graphene and CNT based foams *via* freeze casting

Freeze casting methods have received significant interest over the past decade due to the compelling advantages of inexpensiveness, versatility and one-step process, and they are being successfully adopted to synthesize a variety of porous ceramic, metallic, polymeric and composite materials, including recently reported CNT or graphene-based foams.[28–30] During the freeze-casting process, particles entrapped in the aqueous solution are ejected from the moving solidifying front of the ice crystal and then piled up between the growing columnar or lamellar ice crystals. Fig. 1a presents a schematic of the self-assembly process of nanostructured carbon material based cellular solids, in which individual nanomaterials were ejected from the front of the ice crystal and assembled between the growing columnar or lamellar ice. After the subsequent sublimation of ice crystals by the freeze-drying technique, stable free-standing three-dimensional foams were obtained. To obtain homogeneously dispersed aqueous CNT and/or graphene solutions, the precursors for freeze-casting, CNT and graphite were first oxidized according to a previous study.[26,27] The oxidized CNT (*o*-CNT) and graphene oxide (GO) prepared by us dispersed in water quite efficiently due to the attachment of oxygen-containing groups such as hydroxyl, epoxy and carboxyl (FTIR characterization shown in Fig. S1†). Herein, we

fabricated various nanostructured carbon material based macroscopic foams, including *o*-CNT, GO and *o*-CNT/GO hybrid foams by freeze-casting the corresponding aqueous solutions (Fig. 1a, Experimental section), followed by thermal annealing to remove the oxygen-containing groups, and endow the materials with good electrical conductivity and elasticity.[30] As showed in Fig. 1b and 1c, the macroscopically assembled foams with controlled size (up to 800 cm^3) and shape, such as cubes, cylinders and plates, were readily accessible.

Fig. 2a–2i present typical microscope (SEM) images of all three types of foams, which exhibit anisotropic structural features, longitudinal channel-like morphology and transverse honeycomb-like morphology with the cell dimension in the order of tens of micrometers. The cell walls are slightly corrugated and have a thickness of tens of nanometers. Such a high ratio of channel width to wall thickness, approximately 10^3, produces foams with ultra-low density and extra-high porosity. Consistent with our previous report,[30] the graphene foam shows a morphology of short channels with joint walls along the growth direction, as shown in Fig. 2a. In addition, the polygon pores with defects (as shown by arrows in Fig. 2g) in the walls and edges are observed in Fig. 2d and 2g. Unlike the graphene foam, the CNT foams possess long straight channels without joint walls along the growth direction (Fig. 2b) and polygon pores composed with less-defected cell walls and edges in the cross-section images (Fig. 2h), similar to those of previous reports.[1,8,31] Of particular interest is that by mixing these two types of building blocks together, an optimized structure is obtained in the hybrid foams: ordered honeycomb-like structures with joint walls in the growth direction and less-defected cell walls and edges in the cross-sectional view (Fig. 2c, 2f and 2i).

Earlier works have revealed that the microstructural features of the cellular solids that are as-prepared from the freeze-casting method are governed by complex and dynamic liquid–particle and particle–particle interactions.[32] The particles with different surface chemistry and geometries have a significant effect on the microstructures of the resulting foams.[10,33] Herein, the plate-like geometry of the GO sheets and stronger interaction between the GO sheets with water molecule which attributed to the large amounts of oxygen-containing groups on the sheets, result in steric hindrance during the assembly process. Subsequently, a part of the GO sheets is entrapped in the ice crystal front, which eventually leads to the formation of joint walls in the channels. Moreover, the steric effects on restacking of the sheets also leads to the formation of defects in the walls and junctions between them. Alternatively, spaghetti-like *o*-CNT with lower oxidization degree (see experiment part) has a negligible hindrance effect on the growth of the ice crystal, and hence the morphology of CNT-based foams tends to become ordered structures with good regularity. After combining *o*-CNT and GO components together in aqueous solutions, *o*-CNT tends to adsorb onto the graphene oxide sheets through π-stacking interactions.[34] Thus, the hybrid foam shows a honeycomb-like framework similar to that of neat graphene foam.
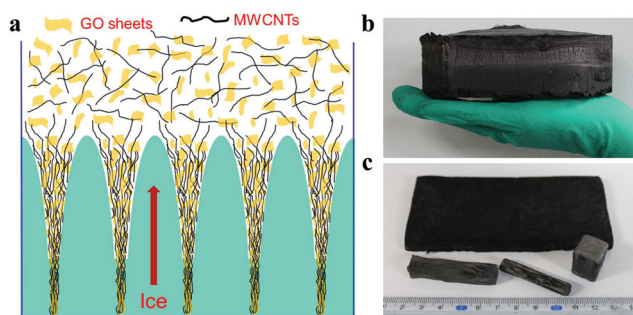

Fig. 1 Illustration of the fabrication technique of foams. (a) When a well-dispersed GO/*o*-CNT dispersion is frozen, nanobuilding blocks are concentrated at the boundary of ice crystals and then aligned along the growth direction of ice due to the squeezing effect. Consequently, stable macrostructures are formed and preserved after freeze drying followed by thermal annealing. Benefiting from the technique, we can prepare samples with different shapes and sizes. Digital images of corresponding samples are presented in (b, c).
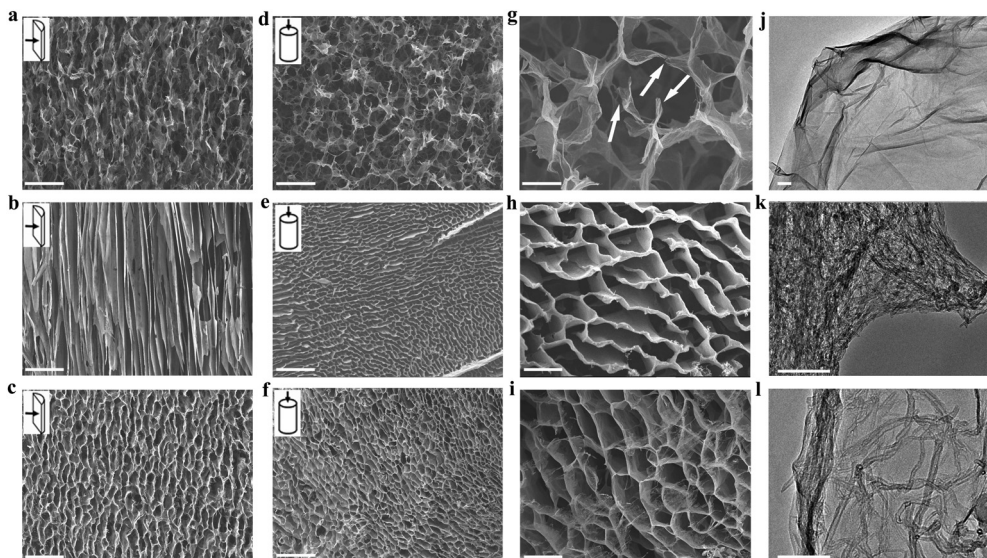
Fig. 2 SEM images showing longitudinal (a) and cross-sectional (d, g) views of the as-prepared graphene foam; white arrows show defects on the walls and junctions in the graphene foam. SEM images of the microstructures of the CNT foam and hybrid foam along the longitudinal direction (b and c, respectively) and in the cross-sectional area (e and f, respectively). In the hybrid foam, the defects are fewer than those in the graphene foam. Moreover, we can find the pull-out CNT bundles. TEM images of the walls in the three types of foams: the cell walls in the graphene foam consisted of wrinkled and overlapped graphene sheets (j); in CNT foams, the walls are spaghetti-like networks with entangled randomly distributed nanotubes (k); and in the hybrid foam, the spaghetti-like CNT networks cover the graphene sheets to form sandwich structures (l). Scale bar in a−f: 100 μm, in g−i: 20 μm, in j and k: 200 nm, and in l: 100 nm.

Mechanical properties

The ability of graphene or CNT based foams to maintain structural integrity upon large deformation is important for the future development of carbon-based flexible materials, ultralight engineering cellular materials (for mechanical damping) and new types of flexible electronic devices. According to our previous work,[30] the foams always show better mechanical compressibility and mechanical stability when the loads are applied perpendicular to the growth (in-plane) direction; thus, the in-plane-direction mechanical performance is particularly explored in this work. Fig. 3a shows the compressive stress–strain curves for all three samples. Curves obtained during the loading process show the three characteristic deformation regimes typically observed in open-cell foams. A linear regime for strain $\leq\sim$10% is generally reflective of the elastic bending of cell walls. Elastic buckling of cell walls is recorded by a plateau regime with gradually increasing slop after plateau strain ($\sim$10%) and a densification regime for strain >$\sim$50% with steeply rising stress.[3] The conventional foams displayed a permanent deformation during the plateau regime, while the graphene foams could hold their elasticity before densification, and irreversible compressive deformation only appears at a large strain (ESI Fig. S3†). The strength of the graphene foam, as quantified by plateau stress at 20% strain to density (1.8–5.4 mg cm^{-3}) ratio, is $\sim$0.11 kPa mg^{-1} cm^{-3}, which is similar to that of graphene based foam found in the literature.[35,36] Compared with the graphene foams, the CNT foams exhibit an intriguing structural compressibility, achieving

nearly full recovery from large strains ($\geq$90%) under uniaxial loading, which is also observed in previous CNT aerogels fabricated with the assistance of a polymer binder.[8] However, the specific strength of the CNT foams is only $\sim$0.01 kPa mg^{-1} cm^{-3}, which is much lower than that of the as-formed graphene foams. Surprisingly, due to synergistic effect of the two types of foams, the CNT/graphene hybrid foam shows the highest specific strength ($\sim$0.35 kPa mg^{-1} cm^{-3}) without any trade-off in the compressibility, as shown in Fig. 3a and S4.† It is worth noting that the weight ratio of the graphene to CNT also has a crucial effect on the mechanical properties. By carefully controlling the ratio between the two components, we found that the hybrid foam in 1 : 1 weight ratio possesses the best mechanical performance, as illustrated in Fig. S5.† Therefore, in the following sections, we only focus on the properties of the hybrid foam with 1 : 1 ratio.

Cyclic tests of hybrid foams with large amplitude (60% strain) were conducted by compression at 0.017 Hz. Fig. 3b shows the identical stress–strain behavior of the foams after 2000 cycles, indicating a slight loss of long-term strength and excellent mechanical stability. Our previous investigation showed that graphene foams experience 6% stress degradation at 60% after only 100 cycles.[30] After the addition of CNT, synergistic effects make the hybrid foams resistant to dynamic loading, and dynamic load bearing capacity is successfully improved. Only $\sim$5% degradation was measured at 60% strain after 1000 cycles in the hybrid foams, in stark contrast to that of CNT/graphene hybrid aerogels with poorly organized structure (12% stress degradation at only 50% strain after 1000
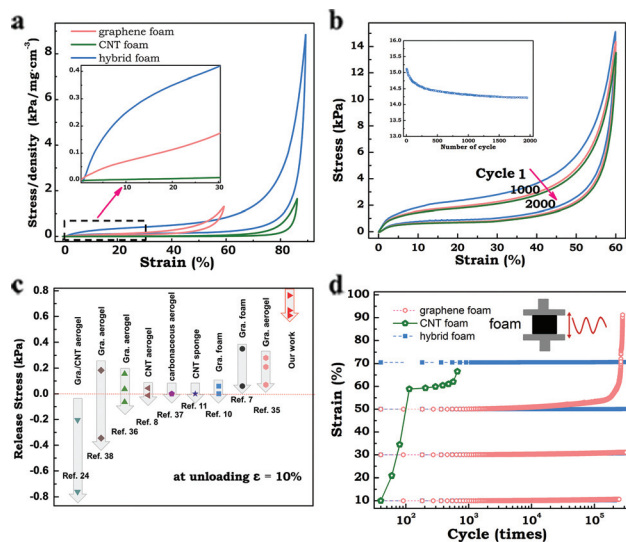
Fig. 3 Characterization of the mechanical properties of the as-formed foams. (a) Stress–strain curves for graphene foam, CNT foam and hybrid foam. The density of the samples is ~6 to ~8 mg cm^{-3}, and the influence of density on the stress–strain curves was investigated in ESI, Fig. S4.† (b) Stress–strain curves of hybrid foam at 1st, 1000th and 2000th cycles during repeated compression to 60%. Inset: stress recorded at 60% strain for 2000 cycles of compression, showing excellent cycle performance of hybrid foam. The compression and release speed is 120% min^{-1}. (c) Comparison of the stress value at 10% strain of hybrid foams and other materials in unloading stress–strain curves during cyclic test. Note that the performance of the most of the materials would be different with different densities and loading directions (anisotropy), and we chose the highest value (best performance) as their load bearing value. The arrows show the decreased stress with increasing cycle numbers. We can find that our samples exhibit a good mechanical stability during the unloading process. (d) The fatigue resistance of the three types of foams at different strain levels. Inset: schematic of compressive cyclic testing. Strikingly, the hybrid foam possesses a considerably good fatigue resistance, even at the set strain of 70%.

cycles) and the neat hierarchical graphene foam (19% stress degradation at 50% strain after 1000 cycles);[10,24] this excellent mechanical stability should be attributed to the hybrid solid constituents and the highly improved structural regularity in our materials.

This excellent load bearing capacity of our hybrid foams could also be displayed in the unloading curves in cyclic tests, in which three characteristic deformation regimes could be observed as well. In contrast, the three regimes disappeared in the unloading stress–strain curves of most of nanostructured carbon based foams or aerogels and the stress would drop to zero or even a negative value during unloading, indicating incomplete elasticity. Fig. 3c shows a comparison of the load bearing capacity of our hybrid foam and other recently reported 3D porous materials, including graphene foams,[10,36] graphene aerogels,[7,35] carbonaceous aerogels,[37] CNT aerogels,[8] CNT sponges,[11] graphene sheets-nanoribbon aerogels[38] and CNT/graphene hybrid aerogels,[24] under cyclic loading. It was found that the hybrid foams show a better unloading perform-

ance when compared with other cellular solids, as shown in Fig. 3d. For instance, for an unloading stress at 10% strain, most of the materials experience severe degradation with increasing number of cycles, while our hybrid foams hold most of the load after 2000 cycles and shows super-elasticity and excellent loading bear capacity, as shown in Fig. 3c.

Dynamically compressive testing with strain amplitude (5%) at 10 Hz was further employed to assess the fatigue performance of these foams at various applied strain levels for at least 2.0×10^5 cycles (Fig. 3d). Despite their excellent compressibility at static compression, due to the low strength and poor load bearing capacity, the CNT foams collapse at low compression strain (10%) after less than one hundred cycles, as evidenced by the large fatigue strain (shrinkage from the original length) in Fig. 3d. Comparatively, the graphene foams showed much better structural robustness and exhibited negligible fatigue strain at low strain level. However, it should be noted that at the set strain of 50%, the shrinkage of the graphene foams begins to increase rapidly after ten thousand cycles, as shown in Fig. 3d, which could be considered as either fatigue failure or degradation. Strikingly, it is found that the fatigue performance of the hybrid foams are remarkably stable, and only 0.61% fatigue shrinkage could be measured after enduring 300 000 cycles at a large strain (70%), highlighting their structural robustness and fatigue resistance. In addition, it is worth noting that our hybrid foams also exhibit a dynamic thermo-mechanical stability, as evidenced by the constant storage modulus over a wide temperature range (−150–350 °C) in Fig. S6†, further promising their practical application as lightweight, robust and elastic cellular materials with stable performance in extreme conditions.

Synergistic mechanism

Because the nanostructured carbon-based macroscopic porous architectures are generally brittle with low mechanical resilience and permanent deformation could usually be observed after severe compression, the exceptional static and dynamic mechanical performance observed in our CNT/graphene hybrid foams is a surprising feature. Previous studies have suggested that when foam made of graphene or CNT based walls is severely compressed, damage to the local microstructure from the collapsing and overwhelming elastic energy due to inter-wall adhesion, such as van der Waals interactions, would prevent elastic recovery, causing the loss of collective elasticity and strength.[10] Indeed, the super-elasticity and mechanical stability could not be observed in the neat graphene foams (Fig. S7, S8c and d†) with poorly ordered structure or graphene/CNT hybrid aerogels with random stacking.[24] We thus believe that in our hybrid materials, the highly organized, hierarchical architectures and the synergistic effects at different levels contribute to this remarkable mechanical performance. By monitoring the deformation process of the hybrid foam, the contributions of every structural level to the improved mechanical stability can be discussed from the following three aspects:
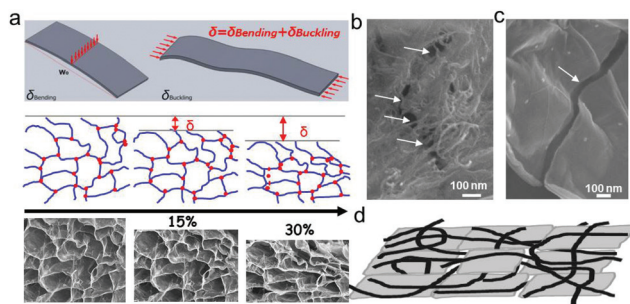
Fig. 4 (a). Schematic description of the unit cell model of the foams and the evolution in cell structure with strain. The foam exhibits uniform deformation. SEM images illustrate the morphology of the cracks on the cell walls. (b) In the hybrid foam, the CNT bundles connect the cleft parts together, while (c) in the graphene foam, a smooth crack is observed, which implies its lower stability. (d) Schematic of the cell walls, which are comprised of stacked graphene sheets and the intercalated spaghetti-like nanotubes.

First, the structural regularity in the hybrid foams allows the homogeneous structural reorganization under increasing compressive strain, as shown in the *in situ* compression SEM images in Fig. 4a. When uniaxial stress is initially applied to the foams such that each cell edge would transfer the force, the structure deformation was activated, and the walls in one cell began bending and buckling. Due to their ordered organization, the structures in the hybrid foams exhibit uniform deformation, whereas the non-uniform distribution of cell size in randomly structured foams leads to inhomogeneous strain and severe local deformation. As shown in Fig. S7 and S8,† both local structural damage and unrecovered deformation are observed in graphene foam, and the hybrid foams in contrast still hold their honeycomb-like structure after 90% compression. In addition, this honeycomb-like manner, in which the nanostructured carbon material based walls are organized, was also considered to be able to maximize the elastic modulus and strength.[10]

Second, the mechanical stability of cell edges was crucially important for assuring the structural compressibility and elasticity under large deformation. According to the structural characterization, as shown in Fig. 2g and S7b,† the presence of apparent defects in cell edges would greatly weaken the strength and stability of the graphene foam. After the incorporation of nanotubes inside the graphene sheets, the defects in edges between neighbouring cell walls in the hybrid foam were significantly reduced (Fig. 2i).

Third, in the hybrid foams, the cell walls are comprised of stacked graphene sheets and spaghetti-like nanotubes, as shown in schematic presented in Fig. 4d. As expected, the nanotubes behave like long and entangled threads, weaving the graphene sheets into continuous structures, which then greatly enhance the microstructure stability of the material under static and dynamic compression. For instance, one of the deformation modes observed in the cell wall depended on crack propagation, as shown in Fig. 4b and 4c. Similar to the

fibrils that induce crack-shielding mechanism in biomaterials, the nanotubes, which interweave in the crack zone and act as fiber bridges, are effective against the propagation of cracks and advances in damage.[39] Moreover, in accordance with the literature,[18,40] we also suggest that mechanical properties, such as the strength and modulus of the solid constituents (cell walls), in the hybrid foams would be enhanced, allowing the van der Waals adhesion to be overcome by the elastic energy. Therefore, the combination of compressibility, super-elasticity and stability performance in our hybrid foams should be attributed to the synergistic effects from the graphene and carbon nanotubes; because of this combination, ordered, multi-scaled hierarchical architectures could be achieved, and both the bending stiffness and damage resistance of the solid constituents in this architecture under compression are improved effectively.

Pressure sensing and application in artificial skin

The graphene and carbon nanotubes construct hybrid foams with not only excellent mechanical properties, but also high electrical conductivity. Four-probe electrical tests indicated that the electrical conductivity of the hybrid foam could reach up to ~0.2 S cm^{-1}, which is close to that of the graphene foam in our previous work,[30] which holds great potential for application as pressure sensors in the fields of smart materials. To demonstrate its sensing capability, the variation of electronic resistance to the applied pressure in different situations was investigated, as shown in Fig. 5a. The resistance variation ratios (defined as $\Delta R/R_0 = (R_p - R_0)/R_0$, where R_0 and R_p denote
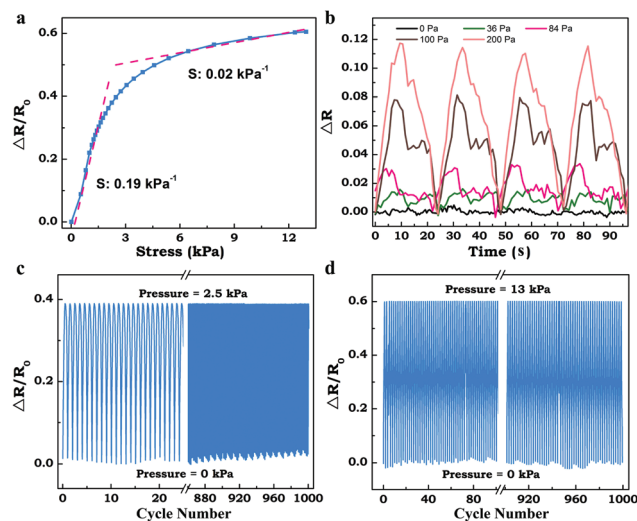

Fig. 5 Characterization of the resistive pressure response of hybrid foam: (a) Electric variation ratio change with applied pressure. The ratio increased exponentially with increased pressure; the sensitivity in the range of 0−2.5 kPa is 0.19 kPa^{-1}, while in the range of 2.5−13 kPa, it is 0.02 kPa^{-1}. (b) Detection limit test on the hybrid foam. The minimum value of the detectable pressure is 36 Pa. The reliability test of hybrid foam under repeated loading and unloading pressure of 2.5 kPa (c) and 13 kPa (d).

the electrical resistance without and with applied pressure, respectively) increased monotonously with the loading at low pressure up to 2.5 kPa, after which the increasing trend of $\Delta R/R_0$ became negligible with applied pressure. The decreased resistance of the hybrid foam during the compression process was mainly due to the different conducting paths and contact resistance between the closely located cell walls. In particular, the pressure sensitivity S (defined as $S = \delta(\Delta R/R_0)/\delta_P$, where P is the applied pressure) is 0.19 kPa^{-1} and 0.02 kPa^{-1} in the 0–2.5 kPa and 2.5–13 kPa range under loading process, respectively. After removing the applied pressure, the electrical resistance completely recovers to its original value, indicating its ability to detect the pressure cyclically. Comparatively, the S value at the lower pressure level is almost one order of magnitude higher than that of a CNT/PDMS sponge ($S = 0.023$ kPa^{-1}) as well as that of a CB/PDMS sponge ($S = 0.046$ kPa^{-1}), according to the literature.[41,42] Moreover, it is comparable to that of a graphene coated PU foam based pressure sensor ($S = 0.26$ kPa^{-1})[43] or complicated micro- or nano-structure pattern based sensors, from 0.55 kPa^{-1} to 8.4 kPa^{-1}.[44,45] (More information is given in Table S1 in the ESI†). However, in the former case, fractures in PU foams are required to improve the pressure sensitivity, which is accompanied by apparent decrease in mechanical stability. For the latter, both the size and shape of the micro-structured rubber layer based core part in the sensors have to be carefully controlled to fulfill their function.

To further investigate the features of the sensor, the resistive responses of the foam to cyclic loading and unloading at set pressures were recorded and plotted in Fig. 5b. It clearly shows that this sensor can detect pressure as low as 36 Pa, which is comparable to the detectable pressure values achieved by other types of pressure sensors (see Table S1†) mentioned in the literature: 3 Pa,[44] 9 Pa,[43] 27 Pa,[46] 2.5 kPa,[47] and 50 kPa.[48] Regarding the potential application as a pressure sensor, the structural stability of the foam is one of the major performances considered. To this end, cycle tests with two different pressure values, namely, 2.5 kPa and 13 kPa, over one thousand times (in Fig. 5c and d) were applied to the sensors. A consistent resistance variation can be maintained during the process, implying the long working life and reliability of the sensors.

In addition, we demonstrated that the as-prepared graphene/CNT hybrid foams can be integrated into a flexible device utilized in artificial skin fields. As illustrated in Fig. 6, the hybrid foams with size of 8 × 8 × 4 mm^3 were attached onto the polyimide (PI) film, which was equipped previously with electrodes to form 4 × 4 pixel arrays. The schematic model and digital image of the sensor are shown in Fig. 6a, 6c and 6e. The boundaries among the individual graphene/CNT foam units were separated by PU foam and sealed by PDMS film. The pressure-sensing mechanism of our device is related to the resistive variation of the foam between the counter electrodes. The equivalent circuit of the obtained electronic sensor is shown in Fig. 6b, in which R_x represents the dynamic resistance of the foam between the electrodes. When the pressure
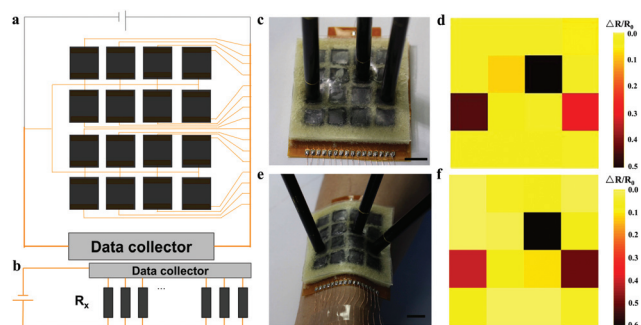

Fig. 6 (a) Schematic model of the artificial skin: the hybrid foams (black squares) were attached to the electrodes (yellow rectangles) and the signals were collected by the data collector. (b) The equivalent circuit of the sensor: R_x represents the dynamic resistance of the hybrid foam during the loading process. (c) Digital images of the artificial skin and three positions compressed to test the pressure-sensing capability. (d) The mapping profile of the pixel signals generated by compression. (e) Digital images of the artificial skin attached on arm and three positions compressed. (f) The mapping profile of the pixel signals generated by the compression. Scale bar: 10 mm.

was applied to the individual arrays in the device, as shown in Fig. 6c, the one to which the pressure was applied exhibited a deformation, leading to a decrease of the local resistance, while the neighbouring arrays, which did not encounter the compression, maintained their initial states. Mapping out the resistive variation of individual arrays would clearly show the pressure distribution in the device, as shown in Fig. 6d, implying its high space resolution and pressure sensitivity. Comparatively, the device configuration in this study exhibited high pressure and spatial sensitivity, which cannot be achieved in the graphene/PU foam based pressure device because of inevitable mutual interference among the units, as reported in Yu's work.[43] Fig. 6e shows that the device can also detect pressures in a bending situation, where both the spatial resolution and pressure intensity are similar to that of the flat situation. In fact, the space resolution is limited by the size of the foam units. In the future, a device with a considerably higher resolution, such as down to micro- or nano-scale, could be achieved *via* the synthesis of tiny foams.

Conclusions

In this study, we successfully fabricated hierarchically structured graphene/CNT hybrid foams through freeze casting methods, followed by thermal reduction. The ideal combination of the two types of nanostructured carbon materials bring about multi-scale synergistic effects in the hierarchical ordered structure, which endows the as-prepared foam with an outstanding mechanical performance, such as super elasticity, compressibility, stability and high mechanical strength. Along with their good electrical conductivity, we revealed the capability of the foams in detecting pressure with high sensitivity and long life time. Equipped with a flexible electric circuit, we

successfully demonstrated their potential as a material for arti-
ficial skin.

Acknowledgements

Notes and references

1 A. Abarrategi, M. C. Gutiérrez, C. Moreno-Vicente,
   M. J. Hortigüela, V. Ramos, J. L. López-Lacomba,
   M. L. Ferrer and F. del Monte, *Biomaterials*, 2008, **29**, 94–
   102.
2 M. Avalle, G. Belingardi and R. Montanini, *Int. J. Impact.
   Eng.*, 2001, **25**, 455–472.
3 L. J. Gibson and M. F. Ashby, *Cellular solids: structure and
   properties*, Cambridge University Press, 1999.
4 M. I. Idris, T. Vodenitcharova and M. Hoffman, *Mater. Sci.
   Eng., A*, 2009, **517**, 37–45.
5 S. Nardecchia, D. Carriazo, M. L. Ferrer, M. C. Gutiérrez
   and F. del Monte, *Chem. Soc. Rev.*, 2013, **42**, 794–830.
6 H. Huang, P. Chen, X. Zhang, Y. Lu and W. Zhan, *Small*,
   2013, **9**, 1397–1404.
7 Y. R. Li, J. Chen, L. Huang, C. Li, J. D. Hong and G. Q. Shi,
   Adv. Mater., 2014, **26**, 4789.
8 J. Zou, J. Liu, A. S. Karakoti, A. Kumar, D. Joung, Q. Li,
   S. I. Khondaker, S. Seal and L. Zhai, *ACS Nano*, 2010, **4**,
   7293–7302.
9 Y. Xu, K. Sheng, C. Li and G. Shi, *ACS Nano*, 2010, **4**, 4324–
   4330.
10 L. Qiu, J. Z. Liu, S. L. Chang, Y. Wu and D. Li, *Nat.
   Commun.*, 2012, **3**, 1241.
11 X. Gui, A. Cao, J. Wei, H. Li, Y. Jia, Z. Li, L. Fan, K. Wang,
   H. Zhu and D. Wu, *ACS Nano*, 2010, **4**, 2320–2326.
12 Z. Chen, W. Ren, L. Gao, B. Liu, S. Pei and H. M. Cheng,
   Nat. Mater., 2011, **10**, 424–428.
13 R. R. Kohlmeyer, M. Lor, J. Deng, H. Liu and J. Chen,
   Carbon, 2011, **49**, 2352–2361.
14 M. B. Bryning, D. E. Milkie, M. F. Islam, L. A. Hough,
   J. M. Kikkawa and A. G. Yodh, *Adv. Mater.*, 2007, **19**, 661–
   664.
15 M. A. Worsley, P. J. Pauzauskie, T. Y. Olson, J. Biener,
   J. H. Satcher and T. F. Baumann, *J. Am. Chem. Soc.*, 2010,
   132, 14067–14069.
16 W. Chen and L. Yan, *Nanoscale*, 2011, **3**, 3132–3137.
17 M. K. Shin, B. Lee, S. H. Kim, J. A. Lee, G. M. Spinks,
   S. Gambhir, G. G. Wallace, M. E. Kozlov, R. H. Baughman
   and S. J. Kim, *Nat. Commun.*, 2012, **3**, 650.

18 Z. D. Huang, B. A. Zhang, S. W. Oh, Q. B. Zheng, X. Y. Lin,
   N. Yousefi and J. K. Kim, *J. Mater. Chem.*, 2012, **22**, 3591–
   3599.
19 Y. W. Cheng, S. T. Lu, H. B. Zhang, C. V. Varanasi and
   J. Liu, *Nano Lett.*, 2012, **12**, 4206–4211.
20 X. C. Dong, J. Chen, Y. W. Ma, J. Wang, M. B. Chan-Park,
   X. M. Liu, L. H. Wang, W. Huang and P. Chen, *Chem.
   Commun.*, 2012, **48**, 10660–10662.
21 X. C. Dong, Y. W. Ma, G. Y. Zhu, Y. X. Huang, J. Wang,
   M. B. Chan-Park, L. H. Wang, W. Huang and P. Chen,
   J. Mater. Chem., 2012, **22**, 17044–17048.
22 W. Wang, S. R. Guo, M. Penchev, I. Ruiz, K. N. Bozhilov,
   D. Yan, M. Ozkan and C. S. Ozkan, *Nano Energy*, 2013, **2**,
   294–303.
23 A. P. Cohn, L. Oakes, R. Carter, S. Chatterjee,
   A. S. Westover, K. Share and C. L. Pint, *Nanoscale*, 2014, **6**,
   4669–4675.
24 H. Sun, Z. Xu and C. Gao, *Adv. Mater.*, 2013, **25**, 2554–2560.
25 Z. Fan, J. Yan, L. Zhi, Q. Zhang, T. Wei, J. Feng, M. Zhang,
   W. Qian and F. Wei, *Adv. Mater.*, 2010, **22**, 3723–3728.
26 L.-Q. L. Yun Gao, S.-Z. Zu, K. Peng, D. Zhou, B.-H. Han and
   Z. Zhang, *ACS Nano*, 2011, **5**, 2134–2141.
27 J. Zhang, H. Zou, Q. Qing, Y. Yang, Q. Li, Z. Liu, X. Guo
   and Z. Du, *J. Phys. Chem. B*, 2003, **107**, 3712–3718.
28 S. Deville, E. Saiz and A. P. Tomsia, *Acta Mater.*, 2007, **55**,
   1965–1974.
29 H. Zhang and A. I. Cooper, *Adv. Mater.*, 2007, **19**, 1529–
   1533.
30 J. Kuang, L. Liu, Y. Gao, D. Zhou, Z. Chen, B. Han and
   Z. Zhang, *Nanoscale*, 2013, **5**, 12171–12177.
31 M. a. J. H. e. María, C. Gutiérrez, J. Manuel Amarilla,
   R. Jiménez and a. F. d. M. M. L. Ferrer, *J. Phys. Chem. C*,
   2007, **111**, 5557.
32 S. Deville, *Adv. Eng. Mater.*, 2008, **10**, 155–169.
33 W. Li, K. Lu and J. Walz, *Int. Mater. Rev.*, 2012, **57**, 37–60.
34 C. Zhang, L. Ren, X. Wang and T. Liu, *J. Phys. Chem. C*,
   2010, **114**, 11435–11440.
35 H. Hu, Z. Zhao, W. Wan, Y. Gogotsi and J. Qiu, *Adv. Mater.*,
   2013, **25**, 2219–2223.
36 S. Barg, F. M. Perez, N. Ni, P. do Vale Pereira, R. C. Maher,
   E. Garcia-Tunon, S. Eslava, S. Agnoli, C. Mattevi and
   E. Saiz, *Nat. Commun.*, 2014, **5**, 4328.
37 X.-L. Wu, T. Wen, H.-L. Guo, S. Yang, X. Wang and
   A.-W. Xu, *ACS Nano*, 2013, **7**, 3589–3597.
38 C. Wang, X. He, Y. Shang, Q. Peng, Y. Qin, E. Shi, Y. Yang,
   S. Wu, W. Xu, S. Du, A. Cao and Y. Li, *J. Mater. Chem. A*,
   2014, **2**, 14994–15000.
39 R. O. Ritchie, *Nat. Mater.*, 2011, **10**, 817–822.
40 Q. Liu, L. Liu, J. Kuang, Z. Dai, J. Han and Z. Zhang, *Nano-
   scale*, 2014, **6**, 6932–6938.
41 J.-W. Han, B. Kim, J. Li and M. Meyyappan, *Appl. Phys.
   Lett.*, 2013, **102**, 051903.
42 M. G. King, A. J. Baragwanath, M. C. Rosamond, D. Wood
   and A. J. Gallant, *Procedia Chem.*, 2009, **1**, 568–571.
43 H. B. Yao, J. Ge, C. F. Wang, X. Wang, W. Hu, Z. J. Zheng,
   Y. Ni and S. H. Yu, *Adv. Mater.*, 2013, **25**, 6692–6698.

44 S. C. B. Mannsfeld, B. C. K. Tee, R. M. Stoltenberg, C. V. H. H. Chen, S. Barman, B. V. O. Muir, A. N. Sokolov, C. Reese and Z. Bao, *Nat. Mater.*, 2010, **9**, 859–864.

45 G. Schwartz, B. C. K. Tee, J. Mei, A. L. Appleton, D. H. Kim, H. Wang and Z. Bao, *Nat. Commun.*, 2013, **4**, 1859.

46 C.-L. Choong, M.-B. Shim, B.-S. Lee, S. Jeon, D.-S. Ko, T.-H. Kang, J. Bae, S. H. Lee, K.-E. Byun, J. Im, Y. J. Jeong, C. E. Park, J.-J. Park and U. I. Chung, *Adv. Mater.*, 2014, **26**, 3451–3458.

47 I. Manunza, A. Sulis and A. Bonfiglio, *Appl. Phys. Lett.*, 2006, **89**, 143502.

48 D. J. Lipomi, M. Vosgueritchian, B. C. K. Tee, S. L. Hellstrom, J. A. Lee, C. H. Fox and Z. Bao, *Nat. Nanotechnol.*, 2011, **6**, 788–792.